Numerical Simulation and Experimental Investigation of the Effect of Three-Layer Annular Coaxial Shroud on Gas-Powder Flow in Laser Cladding

Peijie Lv [a], Ling Jin [a], Binggong Yan [a], Liang Zhu [a], Jun Yao [b], Kaiyong Jiang [a,*]

[a] Fujian Key Laboratory of Special Energy Manufacturing, Xiamen Key Laboratory of Digital Vision Measurement, Huaqiao University, Xiamen 361021, China

[b] Department of Engineering, Design and Mathematics, University of the West of England Bristol, UK

Abstract

Laser cladding is a notable metal additive manufacturing (AM). The outstanding benefit of laser cladding is that the cladding process is more flexible and it can be completed in an open environment. However, oxidation phenomenon of active metals such as titanium alloys will unavoidably clad in the open environment. To solve this problem, a three-layer annular coaxial shroud (TACS) has been designed using computational approach and evaluated by experimental data. A four-stream nozzle of gas-powder computational fluid dynamics (CFD) model was established by employing Euler-Lagrange framework to analyze the powder feeding process. Simulation results show that when the velocities of inner-layer gas of TACS and carrier gas are equal, the powder stream exhibits the best concentration within molten pool area due to the formation of the stable laminar powder stream. When the flared angle of outer-layer gas equals 45°, the vortex toroidal flow moves away from the molten pool and the argon

* Corresponding author.
E-mail addresses: jiangky@hqu.edu.cn (K. Jiang).

fills in the entire cladding region to form a high-quality barrier. The optimized parameters of TACS have been applied to the practical coaxial laser cladding of Ti-6Al-4V (TC4). A single-track cladding sample with lower height to width ratio and lower wetting angle can be observed due to the flattening of the shielding gas. The oxidation is greatly reduced.

Key words: laser cladding, titanium alloys, numerical simulation, three-layer annular coaxial shroud (TACS)

1 Introduction

The laser-based metal additive manufacturing (AM) has been widely applied to major industry such as automotive, aerospace, biomedical and shipbuilding [1-5]. Laser cladding has the outstanding benefit of more flexible and can be completed in open environment. Notably, the laser cladding is a sub-application of metal additive manufacturing.

Laser cladding, a coaxial blown powder direct energy deposition (DED) process which has the advantages of high thermal efficiency, low dilution and excellent metallurgical bonding [6], has been widely adopted for parts repairing, surface modification and net or near net shaped components forming [7-9]. Since the high-temperature molten pool exposed to the open environment, the metals react with atmosphere can hardly be avoided in cladding process. According to Paul et al. [10] and Yamaguchi et al. [11], the atmosphere oxygen reacts with carbon in tungsten carbide-cobalt to create pores in cladding process. Park et al. [12] demonstrated that the vanadium oxide generated at interface region was the main reason of crack and delamination during cladding pure vanadium on titanium substrate. Of note, titanium and titanium alloys, especially Ti-6Al-4V (TC4) as one of the most desirable materials in aerospace, chemistry and medical field is extremely easy to pick-up interstitial elements included oxygen, nitrogen and hydrogen during high temperature cladding process [13]. Moreover, oxygen content, as the main element to distinguish different grades in titanium alloys [14], should be highly concerned.

Ti-6Al-4V (TC4) as a typical $\alpha+\beta$ phase alloy has excellent corrosion resistance, high specific strength and remarkable biocompatibility. It's nominal chemistry composition (wt.%) is 5.5-6.8 Al, 3.5-4.5 V and balanced Ti. However, the Ti and Al in Ti-6Al-4V are both affinity with oxygen, and oxygen as interstitial solution can strengthen the lattice strains by resisting the dislocation motion, leading to embrittlement [15]. Hryha et al. [16] demonstrated that the solubility of oxygen in α-Ti could reach to 33 at.% (atomic percent). Therefore, the oxygen from atmosphere should be shielded as much as possible during cladding process.

A chamber filled with inert gas can be used to inhibit the interaction between the high temperature area and the atmosphere [17-20], but the size of the workpiece is constrained by the size of the chamber. Therefore, more flexible shielding technology such as coaxial shroud is a potential preferred solution using laser cladding [21]. Bermingham et al. [22] used the semi-open coaxial trailing shroud in the additive manufacturing of Ti-6Al-4V thin-wall parts, their method to use the shroud with chamber-like structures could still not completely solve size limitation. Another type of approach is to use coaxial shroud to attach it directly to the laser nozzle and then the inert gas is employed to produce a gas curtain forming an inert atmosphere [23-25]. Harooni et al. [26] used a coaxial auxiliary shielding rig in laser cladding and their results showed that the auxiliary argon gas had a dramatic effect on sample from oxidation and embrittlement. Graf et al. [27] employed a trailing inert gas nozzle to maintain the inert gas atmosphere to rebuild groove by Ti-6Al-4V powder. However, the gas-powder coupling made it difficult to control the appropriate gas flow to ensure the effectiveness of inert gas protection and the efficiency of powder feeding.

For laser cladding, coaxial powder feeding system is the most important component [28, 29], essentially ensuring to form a uniform surface geometry [30, 31]. Because there are difficulties on accurately date collection via experimental measurement process, the numerical simulations have been generally acknowledged as an effective way [32-35]. Cortina et al. [25] and Li et al. [36] designed a single-layer annular coaxial shroud module for coaxial laser cladding, their method exhibits a significant effect on both gas and powder concentrations but research still remains to explore the process mechanism using this type of approach. Currently, the coaxial shrouds are mostly single-layer, and few applications [37] are employed using multi-layer structure. The multi-layer structure can effectively reduce the input gas velocity and extend the protective area than the single-layer structure at the same input flowrate. Therefore, it is worth to be developed.

In this paper, a three-layer annular coaxial shroud (TACS) of coaxial laser cladding was presented. To investigate the influence of gas flow on the powder stream and the relationship between the TACS structure and the behavior of shielding gas, a full-scale of 3D numerical gas-powder CFD model was developed under Euler-Lagrange framework, using Fluent as a model developing platform. On account of the optimized parameters obtained from numerical simulation, TACS was 3D printed and tested via experimental process practically with cladding Ti-6Al-4V powder.

2 Theoretical Model of Gas-Powder Flow

To investigate the distribution of the gas-powder flow in TACS, following assumptions was considered in the simulation

1) The collision of particles is neglected since the volume fraction of powder in this flow is close to dilute flow [38].

2) The process is considered as steady and incompressible.

3) The force due to drag, inertia and gravity are taken into account.

4) The velocity of the particle and gas is considered equal when the particles eject out from the nozzle exit.

5) The two-way coupled discrete phase model is used to consider the effect of particles on powder stream.

6) The Rosin-Rammler [39] model is employed to describe the particle size distribution.

To determine the flow field is laminar or turbulent, the Reynolds number should be calculated. The velocity of central shielding gas is 3.82m/s with correspondent to the designed outlet diameter of 10mm by passing the empirical shielding flowrate of 18L/min. The density and viscosity of argon is shown in Table 1, and the Reynolds number is 2916.99 which is larger than critical value of 2300. Therefore, the standard $k-\varepsilon$ turbulence model was applied for this research which was commonly used in powder nozzle simulation as presented in literatures [30, 34, 35].

2.1 Continuous phase modeling

The governing equation of mass conservation is

$$\frac{\partial\left(\rho_f u_i\right)}{\partial x_i}=0 \tag{1}$$

where ρ_f is the density of local fluid, u_i are the velocity components and x_i is the Cartesian coordinates.

The governing equation of momentum conservation is

$$\frac{\partial}{\partial x_i}\left(\rho_f u_i u_j\right)+\frac{\partial}{\partial x_i}\left(\rho_f \overline{u}_i^{'}\overline{u}_j^{'}\right)=-\frac{\partial p}{\partial x_i}+\frac{\partial}{\partial x_j}\left[\mu\left(\frac{\partial \overline{u}_i}{\partial x_j}+\frac{\partial \overline{u}_j}{\partial x_i}\right)\right]+\rho_f g_i+S_i \tag{2}$$

where indices *i*, *j*=1,2,3 representing x, y and z in a Cartesian coordinate, p is the pressure, $\rho_f \overline{u}_i^{'}\overline{u}_j^{'}$ are the Reynolds stresses, g_i is the acceleration of gravity, and S_i is the source term that represents the coupled momentum transport from particle phase [40], it can be expressed as

$$S_i=\sum_{j=1}^{n_C}\frac{3\mu C_D \mathrm{Re}_p}{4\rho_p D_P^2}\left(\overline{u}_{p,i}-\overline{u}_i\right)\dot{m}_{p,j}\Delta t_j \tag{3}$$

where $\dot{m}_{p,j}$ is the particle mass flowrate for j-th trajectory passing through a cell, Δt_j and n_C are the time step and the total number of particles that pass through the cell during time step of Δt_j, C_D is the drag coefficient, Re_p, D_p and ρ_p are the flow Reynolds number, diameter and density of the particle, $u_{p,i}$ is the velocity of the particle in the i-th direction.

μ is the effective dynamic viscosity of the continuous phase which can be represented by the sum of molecular (laminar) viscosity μ_l and turbulence viscosity μ_t

$$\mu = \mu_l + \mu_t \tag{4}$$

$$\mu_l = \frac{\rho_f V_\infty l}{\mathrm{Re}_f} \tag{5}$$

$$\mu_t = \frac{C_\mu \rho_f k^2}{\varepsilon} \tag{6}$$

Where l is the characteristic length, C_μ is a constant which has a default value of 0.09, k is the turbulence kinetic energy, ε is the turbulence dissipation rate, both are defined in the two-equation $k-\varepsilon$ model below.

The governing equation of turbulence kinetic energy is

$$\frac{\partial}{\partial x_i}\left(\rho_f \bar{u}_j k\right) = \frac{\partial}{\partial x_j}\left(\frac{\mu_t}{\sigma_k}\frac{\partial k}{\partial x_j}\right) + G_k + G_b - \rho_f \varepsilon \tag{7}$$

The governing equation of turbulence dissipation rate is

$$\frac{\partial}{\partial x_i}\left(\rho_f \bar{u}_j \varepsilon\right) = \frac{\partial}{\partial x_j}\left(\frac{\mu_t}{\sigma_\varepsilon}\frac{\partial \varepsilon}{\partial x_j}\right) + C_1 \frac{\varepsilon}{k}\left(G_k + G_b\right) - C_2 \rho_f \frac{\varepsilon^2}{k} \tag{8}$$

$$G_k = \mu_t \frac{\partial \bar{u}_i}{\partial x_j}\left(\frac{\partial \bar{u}_i}{\partial x_j} + \frac{\partial \bar{u}_j}{\partial x_i}\right) \tag{9}$$

$$G_b = -g_i \frac{\mu_t}{\rho_f \mathrm{Pr}_t}\frac{\partial \rho_f}{\partial x_i} \tag{10}$$

where G_k is the rate of production of turbulence kinetic energy due to the mean velocity gradients, G_b is the generation of turbulence kinetic energy due to buoyancy effect, Pr_t is the turbulence Prandtl number, and the coefficients of C_1, C_2, σ_k and σ_ε are prescribed as empirical constants, with correspondent default values at $C_1 = 1.44$, C_2=1.92, $\sigma_k = 1.00$ and $\sigma_\varepsilon = 1.30$, respectively.

2.2 Discrete phase modeling

The equation that governs the movement of a particle with density ρ_P and diameter d_p in the gas stream is

$$\frac{du_{p,i}}{dt} = F_D\left(u_i - u_{p,i}\right) + \frac{\left(\rho_P - \rho_f\right)}{\rho_P} g_i + F_i \tag{11}$$

where u_i is the gas velocity, $u_{p,i}$ is the velocity of the particle, the first term F_D on the equation right hand represents the drag force from gas phase acting on each particle, which can be expressed as

$$F_D = \frac{18\mu}{\rho_p d_p^2} \frac{C_D \operatorname{Re}_p}{24} \tag{12}$$

where Re_p is the so-called particle Reynolds number also known as relative Reynolds number which can be defined by Eq. (13):

$$\operatorname{Re}_p = \frac{\rho_f d_p \left|u_i - u_{p,i}\right|}{\mu} \tag{13}$$

C_D is the drag coefficient expressed by following equation:

$$C_D = a_1 + \frac{a_2}{\operatorname{Re}_p} + \frac{a_3}{\operatorname{Re}_p^2} \tag{14}$$

where a_1, a_2 and a_3 are empirical constants which change with the Re_p [41]. The velocity of the particle can be solved by coupling with kinematic equation as below:

$$\frac{dx_i}{dt} = u_{p,i} \tag{15}$$

Rosin-Rammler model has been used to describe the distribution of particle size written as

$$Y_d = e^{-\left(d_p/\bar{d}_p\right)^n} \tag{16}$$

where Y_d is the mass fraction of the particles with a diameter greater than d_p, $\bar{d}_p$ is the mean diameter and n is the size distribution parameter.

2.3 Species transportation

The species transportation equation can be expressed as

$$\frac{\partial}{\partial t}\left(\rho_f Y_x\right)+\nabla\cdot\left(\rho_f u_i Y_x\right)=-\nabla\cdot J_{x,i} \tag{17}$$

where Y_x is the local mass fraction of species x, and it stands for the mass fractions of argon and oxygen in this study. Since the mass fraction of species must be summed to unity, the mass fraction of nitrogen will be determined by unity to subtract the sum of the argon and oxygen mass fraction. In turbulent flows, the diffusion flux J_i of species x can be written as

$$J_{x,i}=-\left(\rho_f D_{x,m}+\frac{\mu_t}{S_{Ct}}\right)\nabla Y_x - D_{x,T}\frac{\nabla T}{T} \tag{18}$$

where S_{Ct} is the turbulence Schmidt number with a value of 0.7. μ_t is the turbulence viscosity. $D_{x,m}$ is the mass diffusion coefficient for species x in the mixture， which is taken 1.89e-5m^2/s for argon in air [42]. $D_{x,T}$ is the thermal diffusion coefficient, the pure argon is taken 0.0177W/m-k [43] and the air included oxygen and nitrogen is taken 0.0242W/m-k, respectively, and the mixture zone is calculated by $D_{M,T}=\sum_x Y_x \cdot D_{x,T}$.

3 Experimental and Simulation Condition

3.1 Laser cladding equipment and material

The laser cladding setup includes the semiconductor laser (LDM-2500, LaserLine, German), the 6-axis robot (IRB4600, ABB, Switzerland), the consecutive-synchronous powder feeder (RC-PGF-D-2, Nanjing Zhongke Raycham Laser Technology Co., Ltd.) and the coaxial nozzle with four-stream and central shielding port, as seen in Figure 1(a). Argon was used as the carrier and central shielding gas. The properties of TC4 powder, argon and air are shown in Table 1. Scanning electron microscope (SEM, JSM-

IT500LA) was used to observe the morphology of TC4 powder. The high-resolution 3D optical profiler (KEYENCE, VR5000) was used for cladded sample geometry measurement.

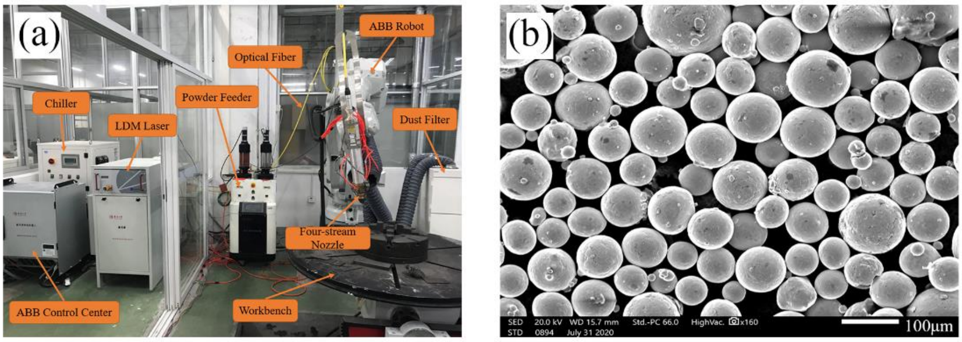

Figure 1. (a) Schematic of equipment and (b) the morphology of TC4 powder.

Table 1. Physical properties of powder and fluid.

Material	Density/(kg/m^3)	Size/(μm)	Viscosity/(kg/m-s)	Oxygen/(%)
TC4	4510	53-150	/	/
Argon	1.6228	/	2.125e-5	0
Air	1.225	/	1.7894e-5	21

The distribution size of TC4 powder is in range of 53-150μm. The flowrate of the powder carrier gas is 10L/min and the central shielding gas is 18L/min. The total flowrate of shielding gas supplied to the TACS is set at 10L/min, 20L/min, 30L/min, 40L/min and 50L/min. A CCD camera (DMK 33UX174, IMAGING, German) was used to determine the velocity of particles according to the following equations,

$$v_p = \frac{d_v}{0.001 \cdot \cos\phi} \tag{19}$$

where v_p is the velocity of the particle (m/s), 0.001 is the exposure time of the camera (s), d_v is the particle moving distance within 0.001s in the direction of axis of TACS, ϕ is the angle between TACS axis and particle moving direction.

3.2 Schlieren setup

For observing the spatial shape of argon flow, a self-developed double-pass schlieren device was used in the experiment. The optical diagram of the schlieren system is presented in Figure 2. Light is emitted from the light source at the focal plane of concave mirror. The light propagation is deflected by different gas densities with different refraction index gradients [44], and the knift located at focal plane is used to shielding parts of light. Finally, the camera is employed to capture different densities of gas in investigation zone using different contrast brightness.

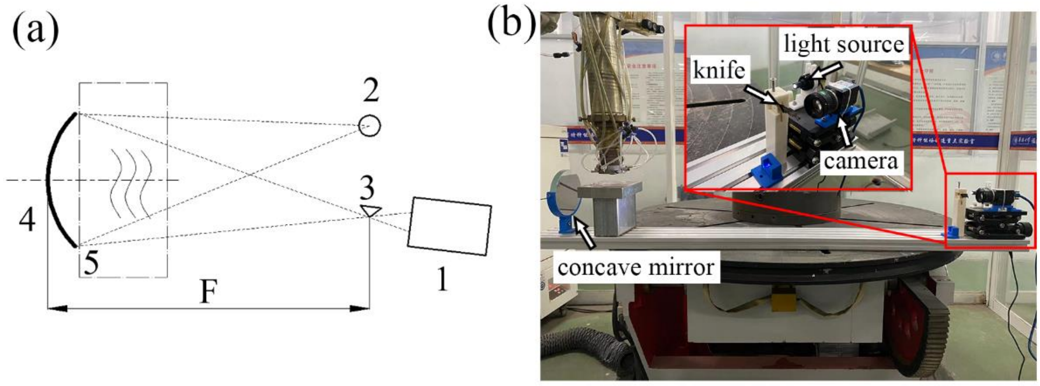

Figure 2. (a) The scheme of schlieren system. 1 – camera; 2 – light source; 3 – Foucault knife; 4 – concave mirror; 5 – investigation zone. (b) Photo of experiments setup.

3.3 Structure of TACS

The feature of three-layer annular coaxial shroud (TACS) can be seen in Figure 3. Three annular gas channels, namely inner-layer, middle-layer and outer-layer gas channels are positioned to surround the coaxial powder feeding channel. The shielding gas enters the TACS through gas inlet that is distributed over horizontal circumferential interval and it admixes in the mixing channel, leading to a uniform outlet gas. The injection direction of annular inner layer shielding gas is parallel to the powder tube at angles, i.e., α=23°, which is intended to assist the powder feeding. The injection direction of the annular middle-layer shielding gas is parallel to the coaxial nozzle to form a gas curtain to prevent air intrusion, and the injection direction of the annular outer-layer shielding gas is flared at an angle β to drive away the air. The candidate values of β are 5°, 15°, 25°, 35°, 45°, 55°.

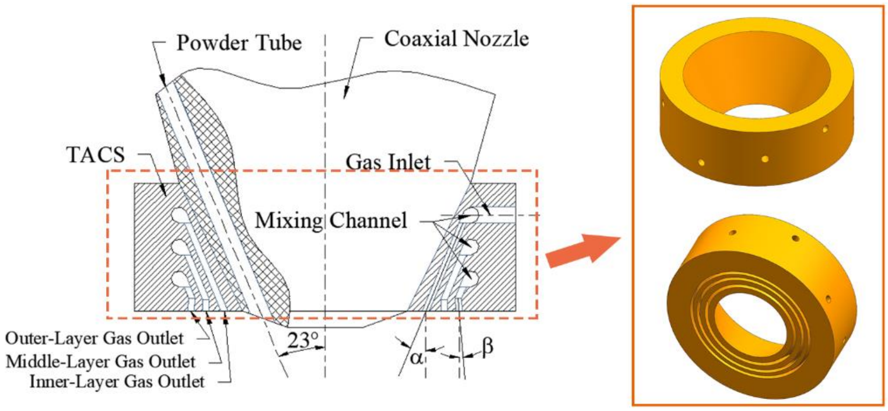

Figure 3. The diagram of assembly cross-section of the TACS.

4 Results and Discussion

4.1 Model validation

In order to give consideration of calculation accuracy and efficiency, the grid independent study was carried out first. A representative computational grid feature is showed in Figure 4. The cylindrical computational domain drawn by $\phi\ 50mm \times L\ 40mm$ is used for mesh convergence study. The green and blue parts are representing central shielding gas and wall respectively, as seen Figure 4(a). The tetrahedral element was adopted to all computational region because the complex geometry feature of the inlet. The grid independent study was done by using coarse, medium and fine mesh volumes, as seen in Table 2. Figure 5 shows that both medium and fine meshes produce consistent data trend of velocity along nozzle axis, indicating the grid convergence can be achieved under fine grid. Figure 4(b) shows computational domain of mesh including the inlet section of TACS configuration. The computational domain is drawn by $\phi\ 100mm \times L\ 20mm$, and the total number of fine mesh volume is 886264. The red, yellow and dark blue parts represent the place inner-, middle- and outer-layer gas outlet of TACS, respectively.

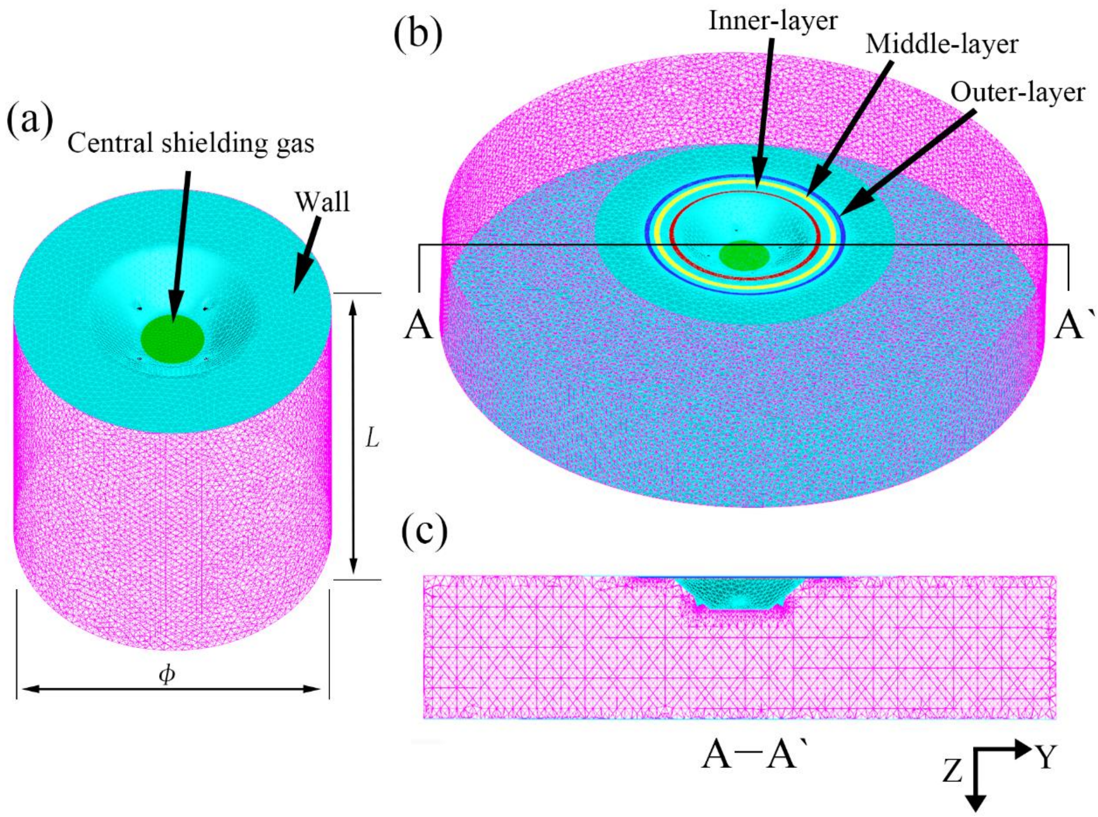

Figure 4. The grid of computational zone: (a) Grid for exploring the powder stream convergence; (b) Grid representing at inlet section of TACS configuration; (c) The cross-section of A-A`, as displayed in (b).

Table 2. Grid densities of different validate cases

Case	Interior cells number	Cells number of central shielding inlet (ϕ10mm)	Cells number of powder inlet (ϕ1.2mm)

Coarse	272612	293	22
Medium	454687	478	40
Fine	864596	1110	85

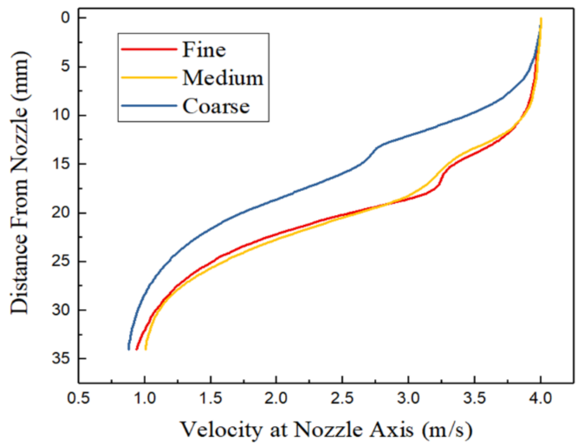

Figure 5. Distribution curve of velocity alone nozzle axis under different grid densities

The convergence study was carried out to compare the mainstream flow over the traveling distance from nozzle. The feeding rate of powder is 8e-3kg/min, 1.26e-2kg/min and 1.62e-2kg/min employed for both simulation and experiment, respectively. Figure 6 shows CFD simulation results and photo images captured by CCD camera for the distribution of powder concentration traveling in space after ejected from nozzle. The four-streams of powder were ejected from the nozzle (consisted 4 powder tubes) to converge in space. Since the CCD camera is completely perpendicular to the nozzle, only two streams are visible (see in Figure 6(a)). Under the same exposure time, the color brightness increasing from darkness to white in corresponding to increase the powder concentration. The powder streams can be divided into three sections, i.e., diffusion zone, convergence zone and divergence zone, as illustrated in Figure 6(b)-Item 1. In the diffusion zone, the powder particles tend to diffusion under the effect of gas diffusion and gravity. The four powder streams meet in the convergence zone with the powder concentration increasing by increasing the powder feeding rate, and the same trends are also evidenced by the simulation results as shown in Figure 6(b). Moreover, when the powder feeding rate is taken at 1.26e-2kg/min, an approximately cylindrical distribution of the powder concentration is favorable for the powder to enter the molten pool evenly as referred by Figure 6(c). The Figure 6(d) compares the powder stream profile for experimental and simulation results at different powder feeding rate. The experimental date and simulation results have consistently shown that the focal distance is about 16.5mm under the exit of nozzle, which incident that the focal distance is slightly influenced by the powder feed rate [45]. The simulation results are in good agreement with experiment measurement.

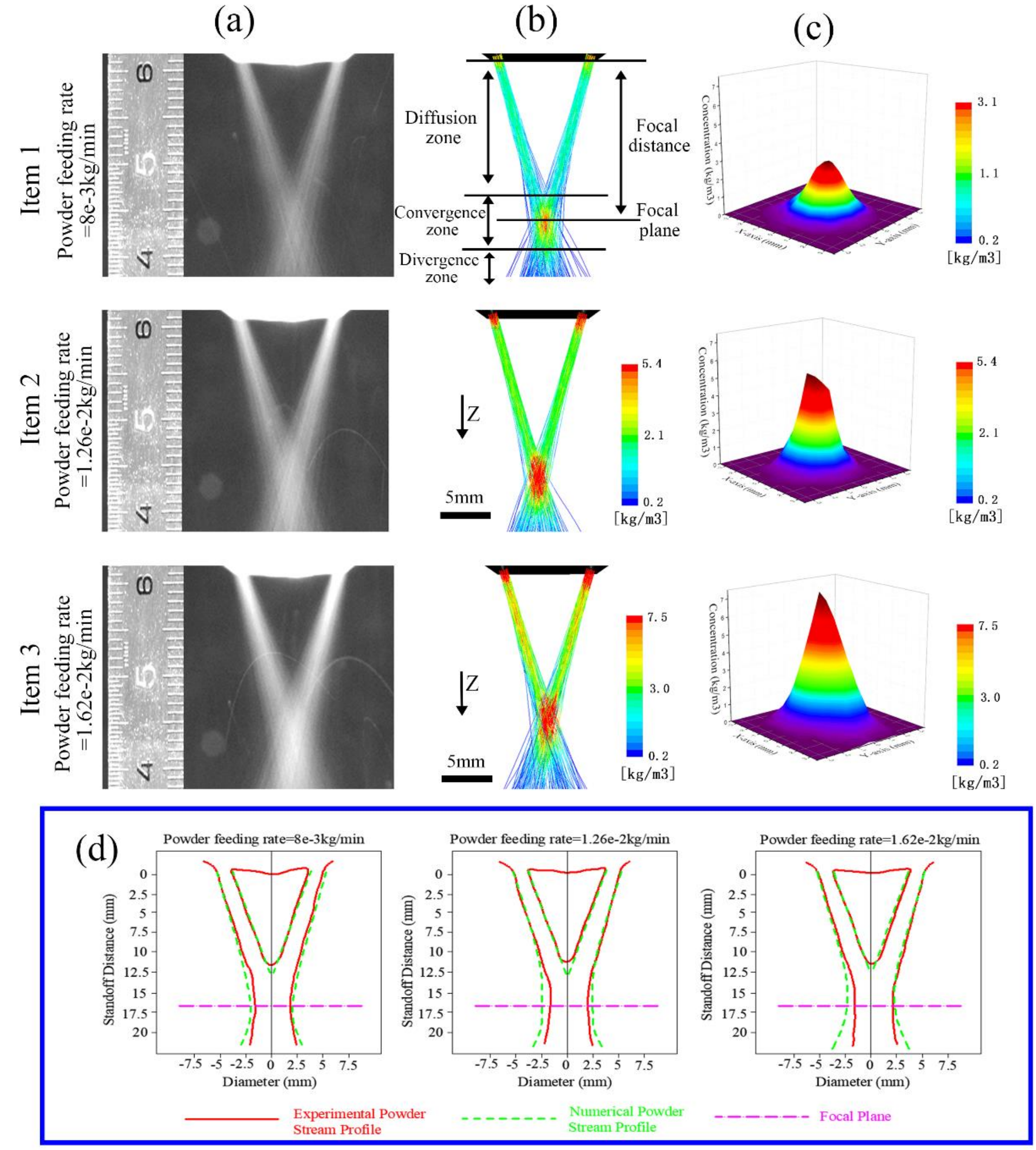

Figure 6. Powder streams convergence effect under different powder feeding rate. From item 1 to item 3, the powder feeding rates are 8e-3kg/min, 1.26e-2kg/min and 1.62e-2kg/min respectively. (a) Captured photos of powder streams; (b) Simulation results of powder concentration; (c) Simulation results of concentration distribution on focal plane. (d) Comparison of experimental and simulation results of powder stream profile by post-processing at different powder feeding rate.

4.2 Comparative analysis on gas flow field with or without TACS

For higher powder utilization, the substrate surface is set at the focal plane. When the argon is injected form the nozzle and shroud, the surrounding argon will immediately come into contact with the air, diffusing under concentration difference while driving the air to move together under the effect by gas viscosity characteristics. According to the law of conservation of momentum, the velocity of surrounding argon will reduce. When the argon arrived the substrate, it spread out and has a tendency to move in the opposition direction. Moreover, the velocity difference between outside and inside of argon (the current relative position is above and below, respectively) make the flow revolves around a curved line under the gas viscosity characteristics to form the vortex toroidal flow. The Figure 7 shows the schlieren visualization of without and with TACS, from which it can be seen that the vortex torodial flow is moved away in the presence of TACS.

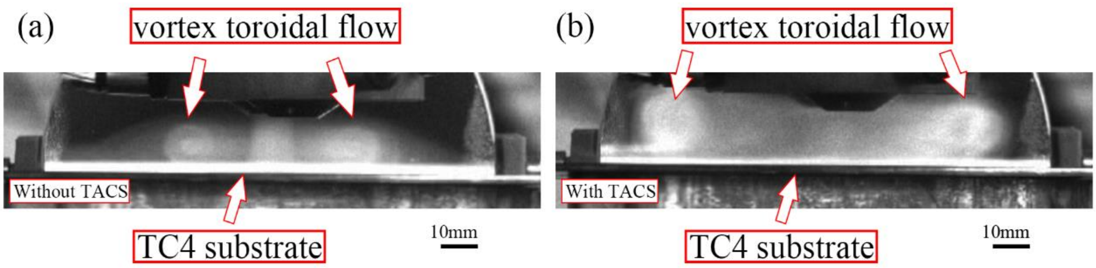

Figure 7. The schlieren visualization of vortex toroidal flow: (a) without TACS, (b) with TACS.

Figure 8 displays the simulation results of velocity field, argon distribution and powder stream of without or with TACS. The numerical simulation as shown in Figure 8(a) and (b) well reflect the phenomenon explored in Figure 7. Figure 8(c) demonstrates the phenomenon that the vortex toroidal flow draws air near the molten pool, diluting the concentration of argon. Then, when the proposed self-developed TACS is attached to the coaxial powder feeding system, a recirculation region has appeared between powder stream and inner-layer shielding gas appears (see Figure 8(b)). However, the

TACS can still contribute to form a more uniform inert gas phase near the molten pool despite the recirculation region appears (see Figure 8(d)). Therefore, the question about whether the stable and dense inert gas shield can be maintained strongly depends on the position of vortex toroidal flow. This influence due to vortex toroidal flow is discussed in literature [46]. Comparing the powder streams results without and with TACS, the higher aggregation of powder streams on the focal plane with TACS. This means that more powders have higher chance of falling into the molten pool using TACS.

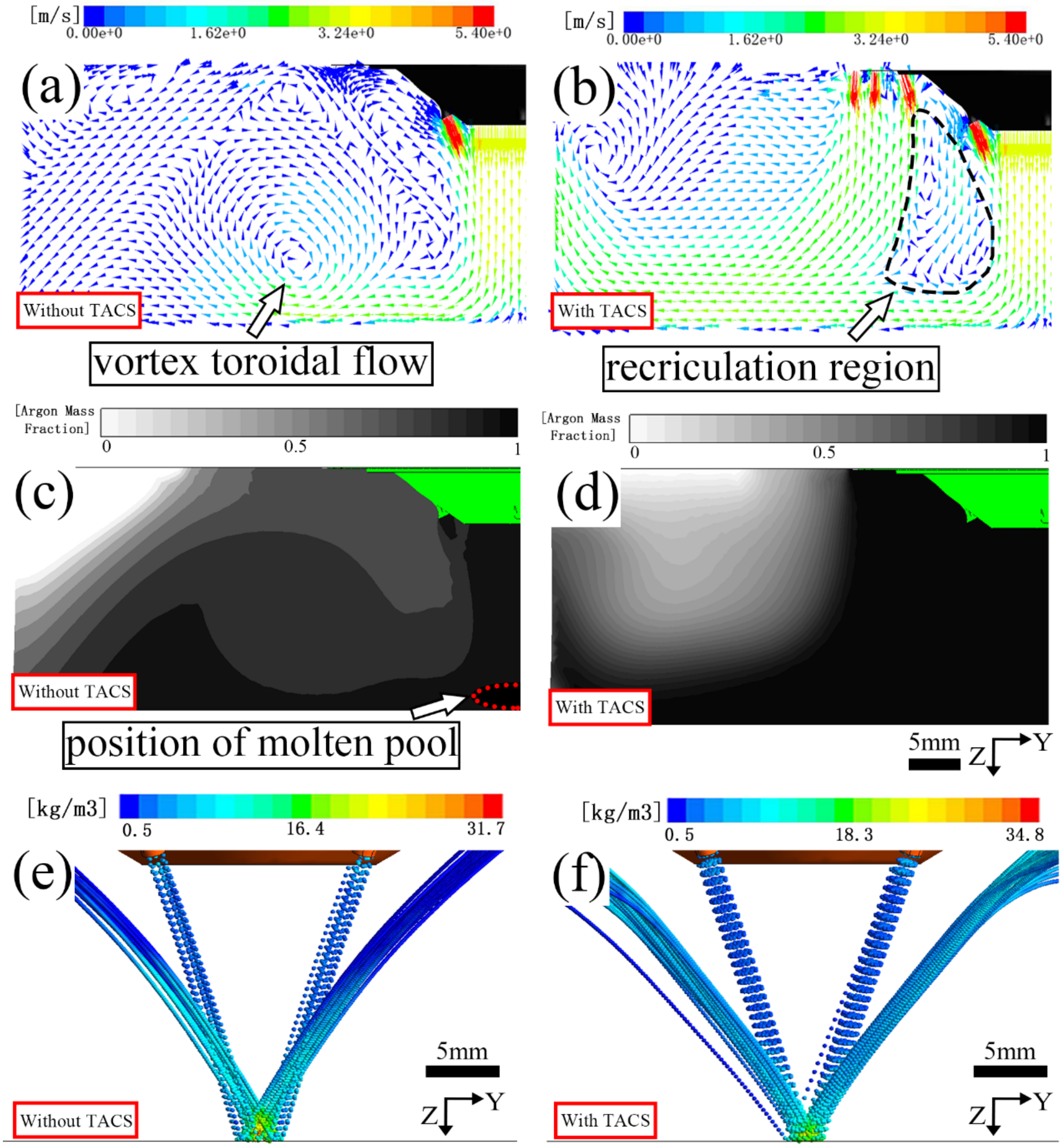

Figure 8. The simulation results of side section of velocity field, argon distribution and powder streams: (a), (c), (e) without TACS; (b), (d), (f) with TACS.

4.3 The effect of the injection gas flowrate

To study the effect of shielding gas with TACS, the injection velocity at the entry of each channel corresponding to different gas flowrate supplied to TACS (see Table 3) is employed in simulation. Powder feeding rate is 1.26e-2kg/min, and the gas injection direction of the outer-layer is fixed at $\beta=5°$. The average velocity of the particles used in simulation is 5.4m/s which is determined by Eq. (19) with data taken via CCD measurement.

Table 3. The shielding gas velocity of inner-, middle- and outer-layer gas outlet under different shielding gas flowrate.

Shielding gas flowrate supplied to TACS(L/min)	10	20	30	40	50
Velocity of Inner-layer(m/s)	1.81	3.63	5.44	7.26	9.07
Velocity of Middle-layer(m/s)	1.51	3.03	4.54	6.06	7.57
Velocity of Outer-layer(m/s)	1.36	2.72	4.09	5.45	6.81

The stable gas curtain is not appeared when the gas flowrate is less than 20L/min (see Figure 9(a) and (b)). When the gas flowrate increases to 30L/min, and moreover, the velocities of inner-layer gas and powder carrier gas are nearly equal, the recirculation region and the stable gas curtain began to appear (see Figure 9(c)). Meanwhile, the vortex toroidal flow moves away from the molten pool. Increasing the gas flowrate to 40L/min (see Figure 9(d)) and 50L/min (see Figure 9(e)), respectively, the characteristics of flow field are similar to that explored in Figure 9c.

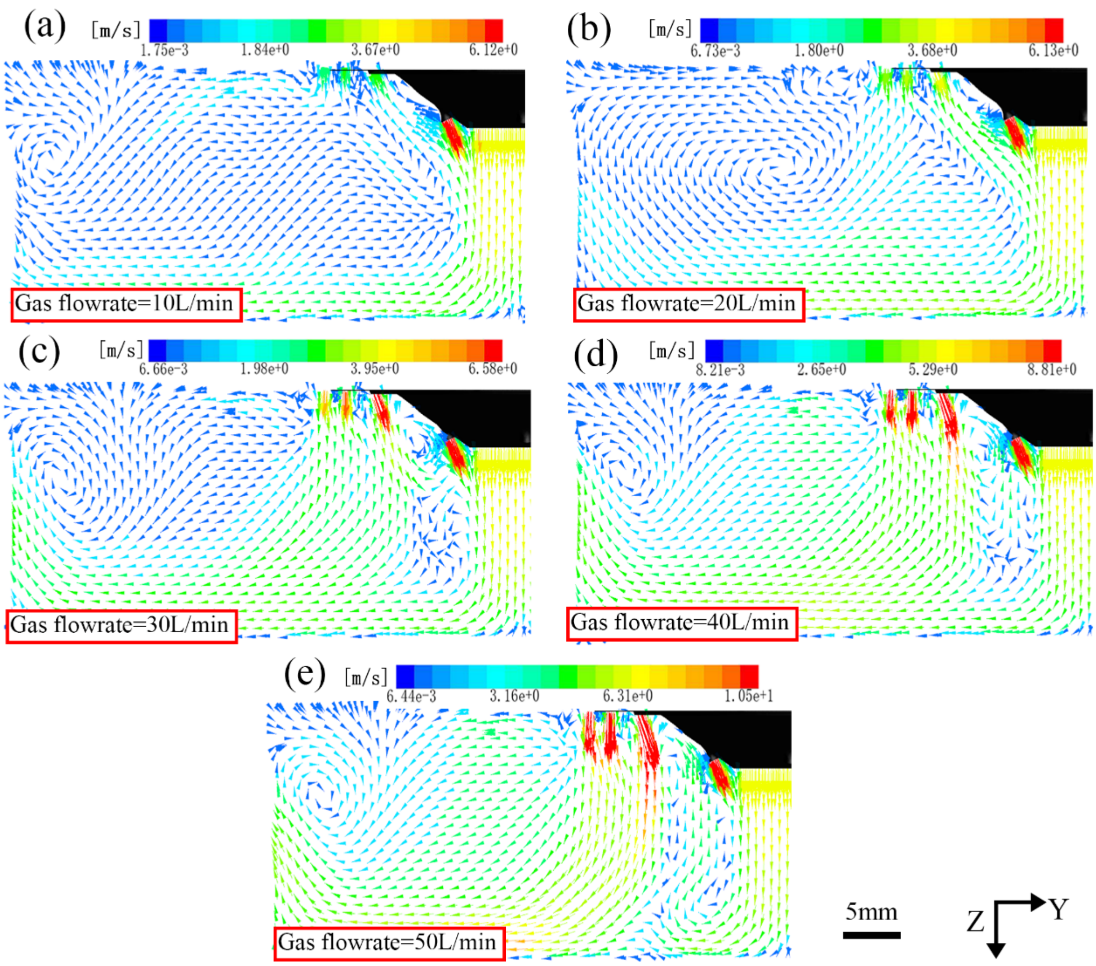

Figure 9. The simulation results of side section of velocity field under different TACS gas flowrate: (a) 10L/min, (b) 20L/min, (c) 30L/min, (d) 40L/min and (e) 50L/min.

Figure 10(a)-(e) show the simulation results of the concentration distributions of the powder particles under different shielding gas flowrate of TACS. The red box area is the position of molten pool. With the shielding gas flowrate increases from 10L/min to 30L/min, the powder particles concentration in the molten pool area increases. However, when the shielding gas flowrate reaches 40L/min and 50L/min respectively, the powder concentration of molten pool area decreases significantly compared to that at 30L/min. The principle of shielding gas affecting on the powder streams depicts a suitable shielding gas flowrate can enhance the laminar transport of carrier gas that would promote powder aggregation at molten pool area to increase the powder utilization. Nevertheless, the stronger shielding gas flow destroys the powder laminar transportation of carrier gas as high-speed gas flow can lead to lower pressure to cause some particles flying away from molten pool. Therefore, the excessive shielding gas will reduce the powder utilization.

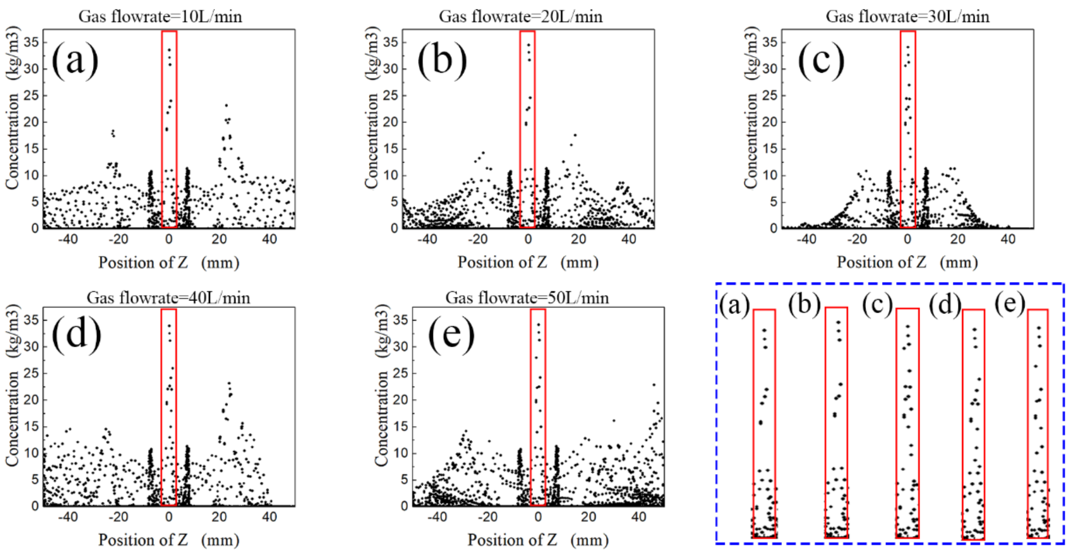

Figure 10. Simulation results of concentration of TC4 powder distributions in the center section of Y-Z plane under different gas flowrate of TACS: (a) 10L/min, (b) 20L/min, (c) 30L/min, (d) 40L/min and (e) 50L/min.

4.4 The effect of the outer-layer injection direction

From data analysis and discussion above, it was known that better protection and powder convergence could be obtained when the velocity of inner-layer gas was equal to the velocity of carrier gas corresponding to shielding gas flowrate of TACS at 30L/min. To further explore the protectiveness, the different flared angle of β=5°, 15°, 25°, 35°, 45° and 55° were used for simulation by keeping flowrate unchanged.

The simulation results of velocity field and argon distribution with different β are showed in Figure 11 and Figure 12 respectively. The vortex toroidal flow is seen to have always kept away from the molten pool. When β=45°, the vortex toroidal flow becomes relative smaller because it is “squeezed” directly by the outer layer shielding gas. A better uniform argon gas phase is then obtained (see Figure 11(e)). By comparion of CFD results given by Figure 11(a)-(e) and Figure 12(a)-(e), the argon distribution in the recirculation region between inner layer shielding gas and carrier gas is kept almost unchanged. When β=55°, the flow dominated by two-vortex appears in the recirculation region between outer layer and middle layer shielding gas (see Figure 11(f)), and the two-vortex flow destroys the uniform distribution of argon due to turbulence effect upon energy dissipation, resulting in poorer protection effect (see Figure 12(f)).

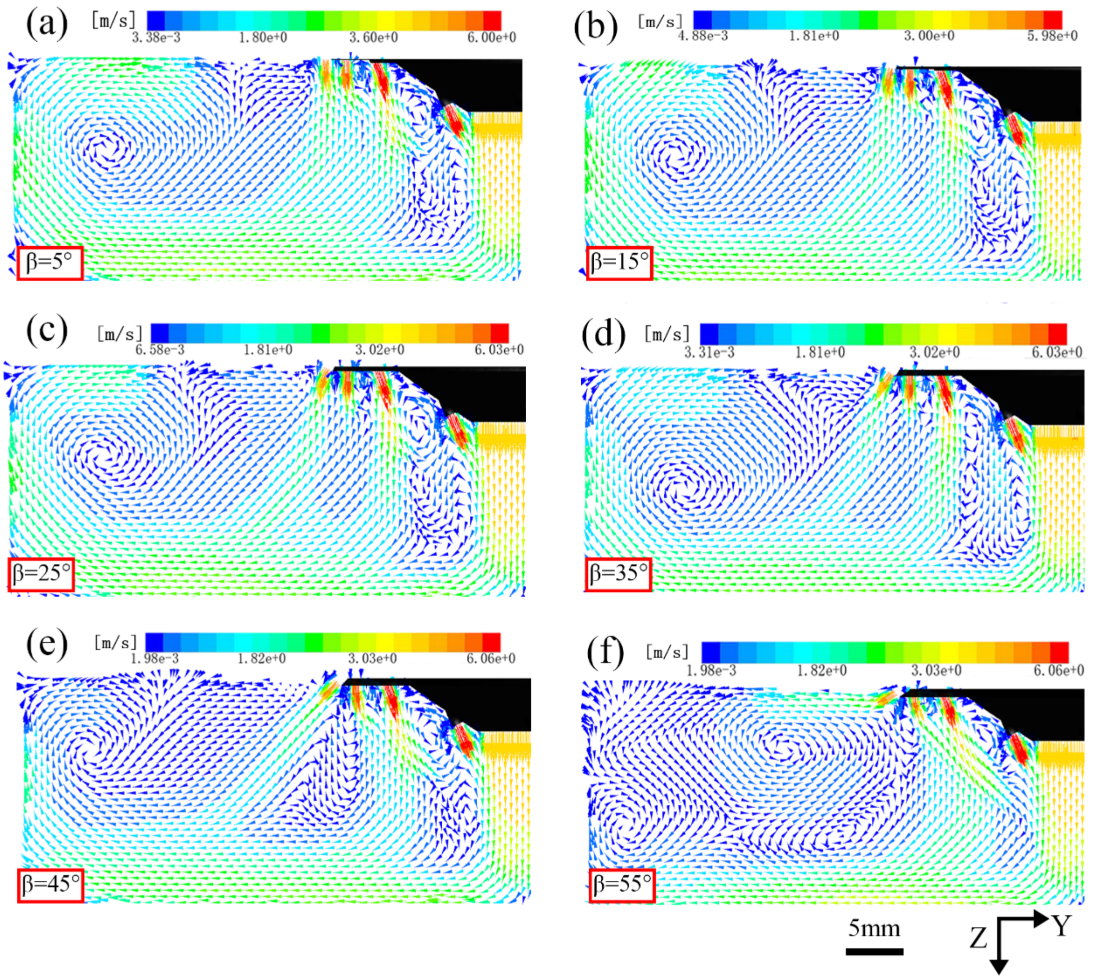

Figure 11. The simulation results of side section of velocity under different TACS flared angle β: (a) 5°, (b) 15°, (c) 25°, (d) 35°, (e) 45° and (f) 55°.

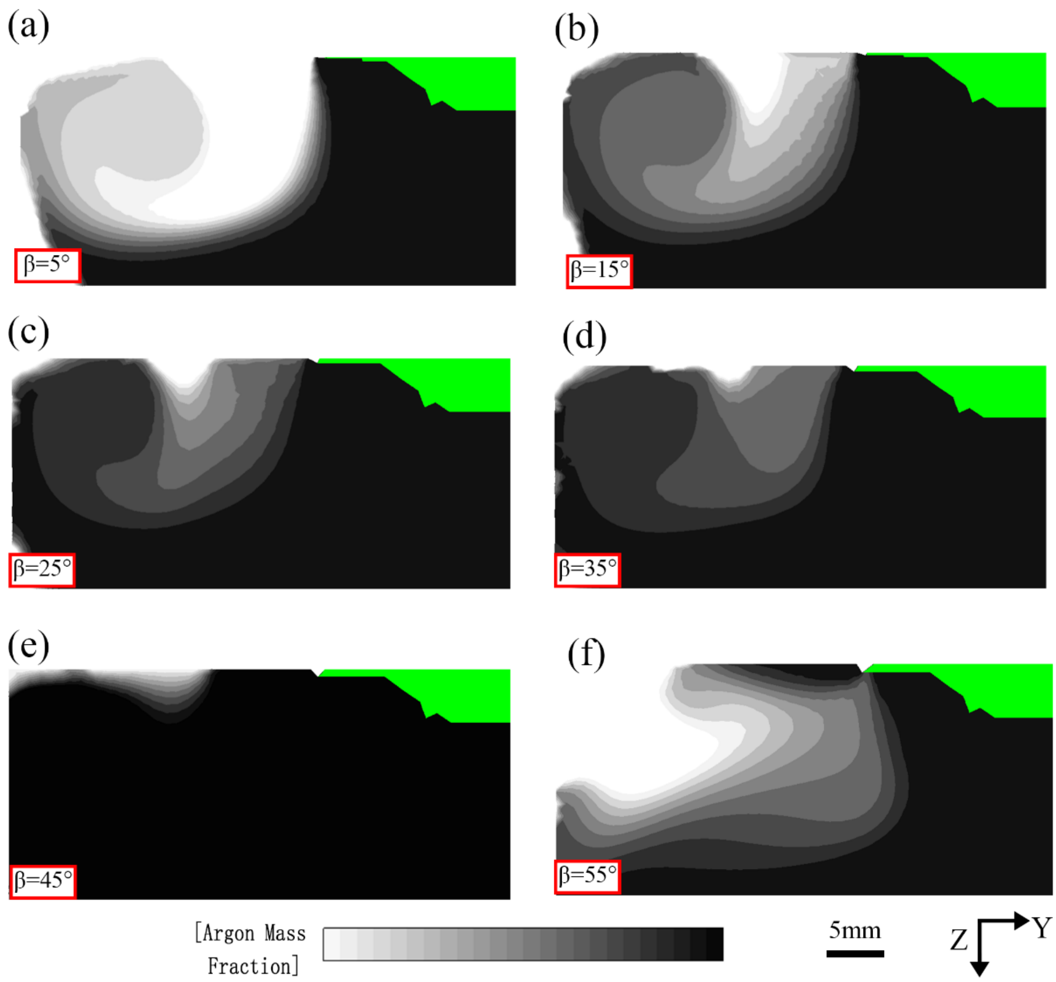

Figure 12. The simulation results of side section of argon distribution under different TACS flared angle β: (a) 5°, (b) 15°, (c) 25°, (d) 35°, (e) 45°and (f) 55°.

4.5 Practical laser cladding test with TACS

Based on the simulation results, TACS was 3D printed at flare angle (β) of 45°. Practical test using laser cladding TC4 with TACS under 30L/min was carried out. According to the discussion of reference [47, 48], the color of titanium alloy oxide layer is associated with the light interference phenomena at the metal-oxide-air interfaces caused by different film thickness. The cladding results (see Figure 13(a)) show that a uniform ivory white oxide film is covered on sample 1 with the usage of TACS, while a fragile brown oxide film is captured on the surface of sample 2 without TACS. This has confirmed that TACS can effectively protect the cladding area from oxidation. Figure 13(b) illustrates the Vickers hardness ($HV_{0.2}$) of track and substrate sections of sample 1 and 2 at 0.2kg loading. As we can see the track hardness of sample 1 is lower than sample 2 from top to bottom because the oxygen is effectively shielded during cladding process. However, the track hardness of sample 1 is still slightly higher than substrate due to thermal stress generated during processing. The further test by employing 3D optical profiler shows that the lower wetting angle decreasing from 64.05° to 60.7° can be obtained with the decrease of height to width ration from 1.946/3.871=0.502 to 1.838/4.837=0.380. The decrease of wetting angle along with height to width ratio can be attributed to the shielding gas simultaneously flattening the molten pool surface, as seen in Figure 14. Table 4 provides the volumes of cladding sample under different shielding gas flowrate at the same powder feeding rate. When the shielding gas flowrate is taken at 30L/min, the sample volume reaches the maximum of 568.584mm^3 with 10.37% increase of proportion, indicating the powder utilization is the highest. Conclusively, the test measurement is consistent with the simulation results.

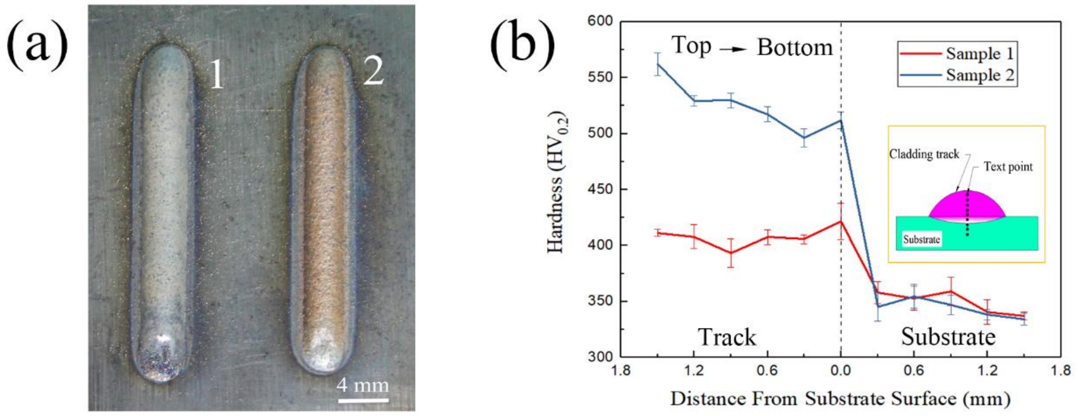

Figure 13. (a) The sample 1 and sample 2 are single cladding using TC4 as powder and substrate with and without TACS respectively. (b) Evolution of the hardness $HV_{0.2}$ of the section of sample 1 and 2 from top to bottom.

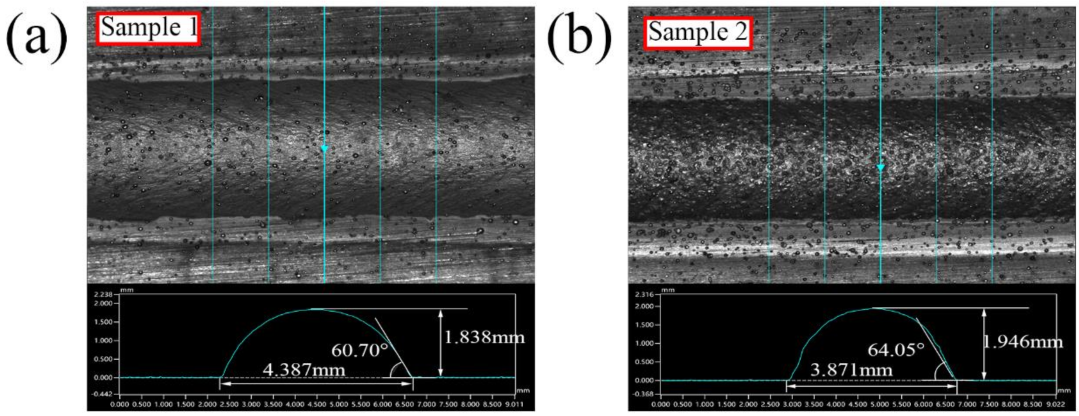

Figure 14. The (a) and (b) are 3D profile and average geometric characteristics of sample 1 and sample 2 respectively.

Table 4. The measured sample volume and proportion increase in volume under different shielding gas flowrate.

Shielding gas flowrate (L/min)	0	10	20	30	40	50
Volume (mm^3)	522.315	550.416	562.608	568.584	561.108	523.920
Increase proportion (%)	--	7.87%	9.52%	10.37%	8.95%	2.44%

5 Conclusions

In this paper, an Euler-Lagrange based numerical simulation model for four-stream powder feeding process was simulated and validated. The effect of the three-layer annular coaxial shroud (TACS) during laser cladding is investigated. The gas flowrate and the structure of TACS were identified as the key influencing factors to predict the velocity field, powder concentration and argon distribution via simulation. Moreover, the optimized parameters were applied to laser cladding experiments. Following conclusions can be drawn from the study:

1) The focus distance of powder streams is about 16.5mm under different powder feeding rates and the experimental and simulation results agree well. Furthermore, an approximately cylindrical powder concentration distribution at focal plane is obtained when the powder feeding rate is at 1.26e-2kg/min.

2) The simulation and schlieren test results show that the vortex toroidal flow has appeared. Moreover, the vortex toroidal flow will draw atmosphere air into argon region, and the use of TACS can effectively move away the vortex toroidal flow.

3）When the velocity of inner-layer of TACS is equal to the velocity of carrier gas, the powder streams show good convergence at the molten pool area. The flared angle β of outer-layer shielding gas has significantly effect on argon distribution, the optimized flared angle of outer-layer is β=45°.

4) The single cladding sample surface color and section hardness test has confirmed that TACS can effectively protect the cladding area from oxidation. The lower height to width ratio (0.502 to 0.380), lower wetting angle (64.05° to 60.7°) and higher powder utilization (maximum 10.37%) depend on the usage of TACS or not.

CRediT Authorship Contribution Statement

Peijie Lv: Conceptualization, Methodology, Validation, Visualization, Formal analysis, Software, Investigation, Data curation, Writing – original draft. **Ling Jin:** Investigation, Data curation. **Binggong Yan:** Conceptualization, Resources. **Liang Zhu:** Investigation, Validation. **Jun Yao:** Conceptualization, Supervision. **Kaiyong Jiang:** Conceptualization, Supervision, Resources, Funding acquisition.

Declaration of Competing Interest

The authors declare that they have no known competing financial interests or personal relationships that could have appeared to influence the work reported in this paper.

Acknowledgement

This work was supported by National Natural Science Foundation of China [51475174] and Subsidized Project for Postgraduates' Innovative Fund in Scientific Research of Huaqiao University.

Reference

[1] X. Dai, H. Xie, Constitutive parameter identification of 3D printing material based on the virtual fields method, Measurement, 59 (2015) 38-43.
[2] D. Herzog, V. Seyda, E. Wycisk, C. Emmelmann, Additive manufacturing of metals, Acta Materialia, 117 (2016) 371-392.
[3] V. Malin, R. Johnson, M. Sciam, Laser Cladding Helps Refurbish US Navy Ship Component, AMPTIAC Quart, 8 (2005) 3-9.
[4] A. Uriondo, M. Esperon-Miguez, S. Perinpanayagam, The present and future of additive manufacturing in the aerospace sector: A review of important aspects, Proceedings of the Institution of Mechanical Engineers, Part G: Journal of Aerospace Engineering, 229 (2015) 2132-2147.
[5] I. Yadroitsev, P. Krakhmalev, I. Yadroitsava, Selective laser melting of Ti6Al4V alloy for biomedical applications: Temperature monitoring and microstructural evolution, Journal of Alloys and Compounds, 583 (2014) 404-409.
[6] E. Toyserkani, A. Khajepour, S.F. Corbin, Laser Cladding, CRC Press, Boca Raton(FL), 2004.
[7] L. Dubourg, J. Archambeault, Technological and Scientific landscape of laser cladding process in 2007,

Surface and Coatings Technology, 202 (2008) 5863-5869.

[8] Z.U. Arif, M.Y. Khalid, E. ur Rehman, S. Ullah, M. Atif, A. Tariq, A review on laser cladding of high-entropy alloys, their recent trends and potential applications, Journal of Manufacturing Processes, 68 (2021) 225-273.

[9] A. Pascu, J.M. Rosca, E.M. Stanciu, Laser cladding: from experimental research to industrial applications, in: Materials Today-Proceedings, 2019, pp. 1059-1065.

[10] C.P. Paul, H. Alemohammad, E. Toyserkani, A. Khajepour, S. Corbin, Cladding of WC–12 Co on low carbon steel using a pulsed Nd:YAG laser, Materials Science and Engineering: A, 464 (2007) 170-176.

[11] T. Yamaguchi, H. Hagino, Effects of the ambient oxygen concentration on WC-12Co cermet coatings fabricated by laser cladding, Optics & Laser Technology, 139 (2021) 106922.

[12] C.W. Park, N.K. Adomako, M.G. Lee, J.H. Kim, J.H. Kim, Interfacial structure and pore formation mechanism during laser cladding of pure vanadium on Ti-6Al-4V alloy, International Journal of Refractory Metals and Hard Materials, 101 (2021) 105671.

[13] X. Li, J. Xie, Y. Zhou, Effects of oxygen contamination in the argon shielding gas in laser welding of commercially pure titanium thin sheet, Journal of Materials Science, 40 (2005) 3437-3443.

[14] E.A. Borisova, Titanium Alloys Metallography, National Defence Industrial Press, Beijing, 1986.

[15] Q. Yu, L. Qi, T. Tsuru, R. Traylor, D. Rugg, J.W. Morris, M. Asta, D.C. Chrzan, M. Minor Andrew, Origin of dramatic oxygen solute strengthening effect in titanium, Science, 347 (2015) 635-639.

[16] E. Hryha, R. Shvab, M. Bram, M. Bitzer, L. Nyborg, Surface chemical state of Ti powders and its alloys: Effect of storage conditions and alloy composition, Applied Surface Science, 388 (2016) 294-303.

[17] P. Wen, Y. Qin, Y. Chen, M. Voshage, L. Jauer, R. Poprawe, J.H. Schleifenbaum, Laser additive manufacturing of Zn porous scaffolds: Shielding gas flow, surface quality and densification, Journal of Materials Science & Technology, 35 (2019) 368-376.

[18] X. Chen, S. Tzeng, W. Wang, Numerical and experimental observations of the flow field inside a selective laser melting (SLM) chamber through computational fluid dynamics (CFD) and particle image velocimetry (PIV), Powder Technology, 362 (2020) 450-461.

[19] D. Huang, H. Li, A machine learning guided investigation of quality repeatability in metal laser powder bed fusion additive manufacturing, Materials & Design, 203 (2021) 109606.

[20] B. Zhang, C. Coddet, Numerical study on the effect of pressure and nozzle dimension on particle distribution and velocity in laser cladding under vacuum base on CFD, Journal of Manufacturing Processes, 23 (2016) 54-60.

[21] R. Poprawe, Tailored light 2, Springer Verlag, Aachen, 2011.

[22] M.J. Bermingham, J. Thomson-Larkins, D.H. St.John, M.S. Dargusch, Sensitivity of Ti-6Al-4V components to oxidation during out of chamber Wire+Arc Additive Manufacturing, Journal of Materials Processing Technology, 258 (2018) 29-37.

[23] J. Sun, Y. Zhao, L. Yang, X. Zhao, W. Qu, T. Yu, Effect of shielding gas flow rate on cladding quality of direct laser fabrication AISI 316L stainless steel, Journal of Manufacturing Processes, 48 (2019) 51-65.

[24] G.P.V. Krishna, V. Vommi, A. Choudhary, G. Muvvala, A study on the effect of molten pool thermal history and gaseous environment in laser surface alloying of AISI 1020 steel with TiN, Optik, 245 (2021) 167758.

[25] M. Cortina, J.I. Arrizubieta, J.E. Ruiz, A. Lamikiz, E. Ukar, Design and Manufacturing of a Protective Nozzle for Highly Reactive Materials Processing via Laser Material Deposition, Procedia CIRP, 68 (2018) 387-392.

[26] A. Harooni, A.P. Gerlich, A. Khajepour, J.M. (Mitch)King, Comparison of nozzle gas shielding

techniques for laser cladding of Zirconium, in: International Congress On Application of Lasers & Electro-Optics, ASM international, Atlanta, Ga, 2015, pp. 404-409.

[27] B. Graf, A. Gumenyuk, M. Rethmeier, Laser Metal Deposition as Repair Technology for Stainless Steel and Titanium Alloys, Physics Procedia, 39 (2012) 376-381.

[28] C. Panwisawas, C. Qiu, M.J. Anderson, Y. Sovani, R.P. Turner, M.M. Attallah, J.W. Brooks, H.C. Basoalto, Mesoscale modelling of selective laser melting: Thermal fluid dynamics and microstructural evolution, Computational Materials Science, 126 (2017) 479-490.

[29] J.I. Arrizubieta, S. Martínez, A. Lamikiz, E. Ukar, K. Arntz, F. Klocke, Instantaneous powder flux regulation system for Laser Metal Deposition, Journal of Manufacturing Processes, 29 (2017) 242-251.

[30] F. Wirth, K. Wegener, Simulation of the multi-component process gas flow for the explanation of oxidation during laser cladding, Additive Manufacturing, 24 (2018) 249-256.

[31] K.Y. Nagulin, F.R. Iskhakov, A.I. Shpilev, A.K. Gilmutdinov, Optical diagnostics and optimization of the gas-powder flow in the nozzles for laser cladding, Optics & Laser Technology, 108 (2018) 310-320.

[32] G. Zhu, D. Li, A. Zhang, Y. Tang, Numerical simulation of metallic powder flow in a coaxial nozzle in laser direct metal deposition, Optics & Laser Technology, 43 (2011) 106-113.

[33] J. Zhang, L. Yang, W. Zhang, J. Qiu, H. Xiao, Y. Liu, Numerical simulation and experimental study for aerodynamic characteristics and powder transport behavior of novel nozzle, Optics and Lasers in Engineering, 126 (2020) 105873.

[34] J. Gao, C. Wu, X. Liang, Y. Hao, K. Zhao, Numerical simulation and experimental investigation of the influence of process parameters on gas-powder flow in laser metal deposition, Optics & Laser Technology, 125 (2020) 106009.

[35] J. Ibarra-Medina, A.J. Pinkerton, Numerical investigation of powder heating in coaxial laser metal deposition, Surface Engineering, 27 (2011) 754-761.

[36] G. Li, J. Zhang, S. Shi, D. Cheng, Mass Distribution of Local Shielding Gas for Laser Cladding of Titanium Alloy in Open Environment, Chinese Journal of Lasers, 46 (2019).

[37] D. Cheng, J. Zhang, T. Shi, G. Li, J. Shi, l. Lu, G. Fu, Microstructure and mechanical properties of additive manufactured Ti-6Al-4V components by annular laser metal deposition in a semi-open environment, Optics & Laser Technology, 135 (2021) 106640.

[38] C.T. Crowe, Review—Numerical Models for Dilute Gas-Particle Flows, Journal of Fluids Engineering, 104 (1982) 297-303.

[39] J. Fan, H. Zhao, K. Cen, An experimental study of two-phase turblent coaxial jets, Experiments in Fluids, 13 (1992) 279-287.

[40] K.E. Babets, Numerical modeling and optimization of waterjet-based surface decontamination, in, New Jersey Institute of Technology, 2001.

[41] S.A. Morsi, A.J. Alexander, An investigation of particle trajectories in two-phase flow systems, Journal of Fluid Mechanics, 55 (1972) 193-208.

[42] Air - Diffusion Coefficients of Gases in Excess of Air, in, https://www.engineeringtoolbox.com/air-diffusion-coefficient-gas-mixture-temperature-d_2010.html.

[43] Argon – Boiling – Melting Point – Thermal Conductivity – Expansion, in, https://material-properties.org/argon-thermal-properties-melting-point-thermal-conductivity-expansion/.

[44] K.Y. Nagulin, D.S. Akhmetshin, A.K. Gilmutdinov, R.A. Ibragimov, Three-dimensional modeling and schlieren visualization of pure Ar plasma flow in inductively coupled plasma torches, Journal of Analytical Atomic Spectrometry, 30 (2015) 360-367.

[45] E. Ferreira, M. Dal, C. Colin, G. Marion, C. Gorny, D. Courapied, J. Guy, P. Peyre, Experimental and

Numerical Analysis of Gas/Powder Flow for Different LMD Nozzles, Metals, 10 (2020) 667.
[46] O.B. Kovalev, I.O. Kovaleva, I.Y. Smurov, Numerical investigation of gas-disperse jet flows created by coaxial nozzles during the laser direct material deposition, Journal of Materials Processing Technology, 249 (2017) 118-127.
[47] S. Wang, Z. Liao, Y. Liu, W. Liu, Influence of thermal oxidation temperature on the microstructural and tribological behavior of Ti6Al4V alloy, Surface & Coatings Technology, 240 (2014) 470-477.
[48] D.P. Adams, R.D. Murphy, D.J. Saiz, D.A. Hirschfeld, M.A. Rodriguez, P.G. Kotula, B.H. Jared, Nanosecond pulsed laser irradiation of titanium: Oxide growth and effects on underlying metal, Surface and Coatings Technology, 248 (2014) 38-45.